A nullspace-based force correction method to improve the dynamic performance of cable-driven parallel robots

Marc Fabritius, Guillermo Rubio-Gómez, Christoph Martin, João Cavalcanti Santos, Werner Kraus, Andreas Pott

Highlights

A Nullspace-Based Force Correction Method to Improve the Dynamic Performance of Cable-Driven Parallel Robots

Marc Fabritius, Guillermo Rubio Gomez, Christoph Martin, João Cavalcanti Santos, Werner Kraus, Andreas Pott

- A force control method in the nullspace of cable-driven parallel robots is presented.
- It aims to keep the cable forces close to a specified level and within their bounds.
- These goals are quickly achieved, despite disturbances or high platform velocities.
- It requires 79% less computational effort than other similar-performing controllers.

A Nullspace-Based Force Correction Method to Improve the Dynamic Performance of Cable-Driven Parallel Robots

Marc Fabritius[a], Guillermo Rubio Gomez[b], Christoph Martin[a], João Cavalcanti Santos[c], Werner Kraus[a], Andreas Pott[d]

[a] *Fraunhofer Institute for Manufacturing Engineering and Automation IPA, Stuttgart, Germany*
[b] *School of Industrial and Aerospace Engineering, Toledo, Spain*
[c] *LIRMM, University of Montpellier, Montpellier, France*
[d] *ISW, University of Stuttgart, Stuttgart, Germany*

Abstract

Cable-driven parallel robots distinguish themselves from other robot types through their large workspace and high dynamic capabilities. Investigations show that with purely kinematic control schemes, the theoretical workspace of such robots cannot be fully realized in practice. Current control methods usually rely on complex models whose parameters are difficult to determine with the required precision or feedback from expensive sensors that can measure the actual platform pose. This work presents a force control method that enables high dynamic capabilities within a large workspace for redundantly-constrained cable-driven parallel robots in practice, without the aforementioned drawbacks. The new method modifies the cable forces within the nullspace of the robot's structure matrix to keep them within their feasible limits and as close as possible to a desired level without changing the platform's pose. In simulation, it achieves similar performance as a state-of-the-art model predictive control method, with 79% less computational effort. Experiments show that it can quickly reject disturbances and is significantly better at keeping the cable forces within their limits on highly dynamic trajectories than a purely kinematic control scheme.

Keywords:
cable-driven parallel robots, force control, redundancy resolution, wrench-feasible workspace

1. Introduction

Cable-Driven Parallel Robots (CDPRs) belong to a family of parallel robots in which cables replace rigid links that hold the platform. The position and orientation of most CDPRs' platforms are controlled by varying the lengths of their cables. A common way to do this is coiling them onto winches [1]. Since this works well even for long cables, which represent relatively lightweight links, CDPRs can have a large workspace, high dynamic performance, and a good payload-to-weight ratio. These benefits set them apart from other types of robots. Another difference is that the portion of a CDPR's workspace accessible in practice not only depends on its geometric parameters but also on the cable force distribution induced by the controller. The cable forces must be kept between a lower and an upper limit to prevent malfunctioning or damaging the robot due to excessive forces or coiling errors. The wrench-feasible workspace of a CDPR is defined as the set of platform positions and orientations (this tuple is called the platform pose hereafter) where its wrench equilibrium can be satisfied for a given set of external wrenches using cables forces within predefined limits [2]. CDPRs with more cables than degrees-of-freedom of their platform are classified as redundantly-constrained CDPRs [3]. For such CDPRs, finding feasible cable force distributions is an underdetermined problem with multiple solutions.

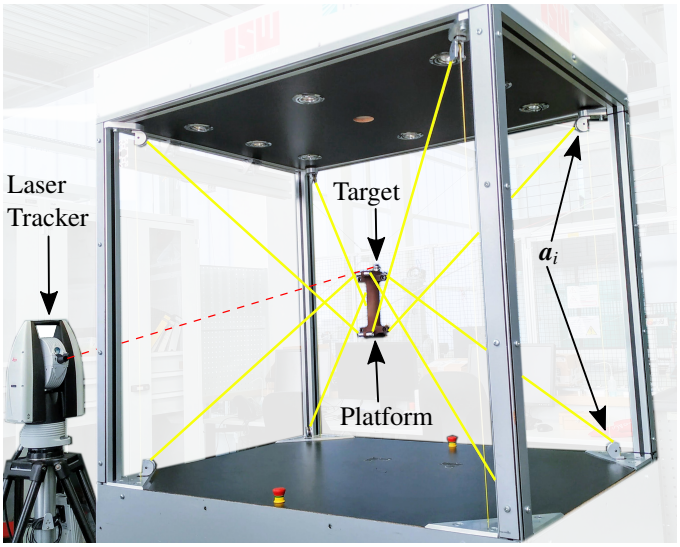

Figure 1: IPAnema Mini CDPR and Laser Tracker

An example from this group of CDPRs is the IPAnema Mini [1, page 398]. It is used to conduct the simulations and experiments in this work and is depicted in Figure 1.

In practice, CDPRs often cannot fully access their theoretical wrench-feasible workspace. This can be caused by errors in the model parameters or unmodelled effects like cable creep, preventing CDPR controllers from obtaining a feasible force

Email address: marc.fabritius@ipa.fraunhofer.de (Marc Fabritius)

distribution, even though one exists.
This makes designing controllers for CDPRs challenging, as it requires weighing between two main objectives: guaranteeing the feasibility of the cable force distribution or controlling the platform pose. For controlling the platform pose, the different methods found in CDPR literature can be broadly divided into two main strategies: control in the operational space (i.e. the platform pose) and control in the joint space (i.e. the cables' lengths). For control strategies in the operational space, the error between the actual and desired platform pose is used as input to the controller. Its output is applied to the platform through separate force controllers for each joint. Multiple works combine this control architecture with different types of controllers such as PID [4], adaptive dual-space controllers [5], H_∞ controllers [6], sliding-mode controllers [7, 8, 9], or exact linearization techniques [10].
To enable control in the operational space, the actual platform pose must be measured by means of cameras [11, 6, 12, 13], lasers [14, 10], or estimated from the effective cable lengths processed through the forward kinematic model of the robot as in [15, 16, 4, 17, 18, 19, 20].
Joint space controllers map the desired platform pose into the joint space using an inverse kinematic model. The resulting commands are fed to controllers that move the winches accordingly and receive feedback on the actual joint positions from their encoders. Some control approaches used in the joint space include proportional-differential controllers [21], wave-based control [22], impedance control [23], synchronization [24] and adaptive control [5]. Due to the constantly changing payloads applied to each winch and the non-linear dynamics of CDPRs, feed-forward linearization of the non-linear terms in the dynamic model, is a common technique used in the joint space control of CDPRs (e.g. [25, 26, 27, 24, 28]).
Most of the previously mentioned approaches perform dynamic control of the torque generated by the winches. Some of them rely on the knowledge of the dynamic models of the CDPR's platform and winches to perform some compensations through dynamic inversion or feed-forward linearization techniques. Alternatively, servomotors can be used in many applications, as they provide robust and high-performance motor position control. In such settings, the dynamics of the actuators can be ignored as the motors can reliably control the cable lengths in the joint space. This simplifies the control scheme of CDPRs, as only an inverse kinematic model has to be implemented.
A drawback of this simple approach is that it cannot explicitly control the cable forces. Its ability to access a CDPR's entire wrench-feasible workspace in practice is therefore often limited. This phenomenon and a possible solution are discussed in the authors' prior work [29].
Regardless of whether the position control is performed in the operational or in the joint space, the cable forces have to be kept within their limits. A common approach for redundantly restrained CDPRs is to employ hybrid position-force controllers. Hereby, feasible force distributions are obtained through redundancy resolution techniques based on the robot's structure matrix and its nullspace (e.g. [26, 30, 4, 31, 32, 21]). The obtained force distribution is then employed along with a dynamic control strategy to control the platform position and guarantee cable force feasibility simultaneously. Due to the non-linear nature of the underlying mathematical problem, most of these approaches employ iterative algorithms as in [33, 34, 35] and some of them [26, 16, 35, 36] are only able to deal with CDPRs with a maximum degree of redundancy of two. Mattioni et al. resolve the redundancy of CDPR by splitting their cables into two sets that are position and force controlled, respectively [37]. The choice of this partition is based on a force sensitivity index to minimize the errors in the cable force distribution.
Santos et al. introduce model predictive control (MPC) methods that compute the set of desired cable tensions as the solution of an optimal control problem considering a dynamic model of the CDPR [19, 20]. The goal of their controllers is to minimize a combination of the error in the platform pose, the variation of the cable forces, and their norm. The feasibility of the resulting cable forces is formulated as an explicit constraint to the optimization problem.
All previously discussed control methods from the literature, which achieve high performance, either rely on the direct feedback of the platform pose or use complex models, which depend on the knowledge of various model parameters. The drawbacks of these approaches are that suitable sensors are often prohibitively expensive, complex models have high computational costs, and their parameters can be difficult to measure with the required precision or may be subject to change in practice, e.g. the cables' stiffness or the platform's mass.
In prior research leading up to this work, [29], a novel force correction method for redundantly-constrained CDPRs, which does not require knowledge of any cable or platform weight parameters, is presented. It relies on servomotors for control in the joint space and modifies the cable forces within the nullspace of the CDPR's structure matrix to keep them inside their limits. A systematic study of its performance throughout the static workspace of the IPAnema 3 CDPR [1, page 395] shows that the method can significantly extend the workspace portion that can be accessed in practice when compared to a kinematic control method.
This work introduces a further development of this method, which additionally aims to keep the cable forces close to a specified level. This new feature could be used to adjust the stiffness of the platform. A new practical tuning procedure enables the method to achieve a high performance in disturbance rejection and on dynamic trajectories. The new method is compared to the MPC approach from [20] in simulation and to a purely kinematic controller in experiments on the IPAnema Mini CDPR. These comparisons cover the full range of the CDPR's dynamic capabilities, showing its ability to reject disturbances and its behavior on three trajectories for various velocities.
The rest of this work is organized as follows. Section 2 introduces the notation and a dynamic model of CDPRs. The new control method and a practical tuning procedure are presented in Section 3. In Section 4, it is evaluated through simulations and experiments and compared to state-of-the-art controllers in terms of disturbance rejection and on dynamic trajectories with various platform velocities. Finally, the conclusion and outlook are given in Section 5.

2. Notation and Modelling of CDPR

Let m denote the number of cables and n the degrees-of-freedom of a CDPR. Each cable $i \in \{1, ..., m\}$ of a CDPR originates from a proximal anchor point $\boldsymbol{a}_i \in \mathbb{R}^3$, given in the fixed robot coordinate system $\mathcal{K}_0$, and connects to a distal anchor point on the moving platform, which is denoted as $\boldsymbol{b}_i \in \mathbb{R}^3$ in the platform coordinate system $\mathcal{K}_p$. The CDPR's n degrees-of-freedom usually consist of its platform position $\boldsymbol{r} \in \mathbb{R}^3$ and rotation matrix $\boldsymbol{R} \in \mathrm{SO}(3)$ expressing its orientation for $n = 6$. As a tuple, they are called the pose $(\boldsymbol{r}, \boldsymbol{R}) \in \mathrm{SE}(3)$ of the platform and determine the mapping between the coordinate systems $\mathcal{K}_0$ and $\mathcal{K}_p$. The location of $\boldsymbol{b}_i$ can be expressed in $\mathcal{K}_0$ as $\boldsymbol{r} + \boldsymbol{R}\boldsymbol{b}_i$.
The state of the platform within its $n = 6$ degrees-of-freedom is parameterized by a vector $\boldsymbol{x} \in \mathbb{R}^6$, whose first three components are the platform position $\boldsymbol{r}$ and the remaining three are a parameterization of the rotation matrix $\boldsymbol{R}$.
The cables of the CDPR are assumed to be straight lines, and their mass is neglected. Their lengths are collected in the vector $\boldsymbol{l} = \begin{bmatrix} l_1 & \cdots & l_m \end{bmatrix} \in \mathbb{R}^m$. For each cable $i \in \{1, ..., m\}$, the vector connecting its endpoints $\boldsymbol{d}_i \in \mathbb{R}^3$, its direction $\boldsymbol{u}_i \in \mathbb{R}^3$ and length $l_i \in \mathbb{R}$ are calculated as

$$\boldsymbol{d}_i = \boldsymbol{a}_i - \boldsymbol{r} - \boldsymbol{R}\boldsymbol{b}_i\,, \qquad \boldsymbol{u}_i = \frac{\boldsymbol{d}_i}{\|\boldsymbol{d}_i\|}\,, \qquad l_i = \|\boldsymbol{d}_i\|\,. \tag{1}$$

Figure 2 shows the relationships of these vectors. Elements in the platform coordinate system $\mathcal{K}_p$ are colored blue.

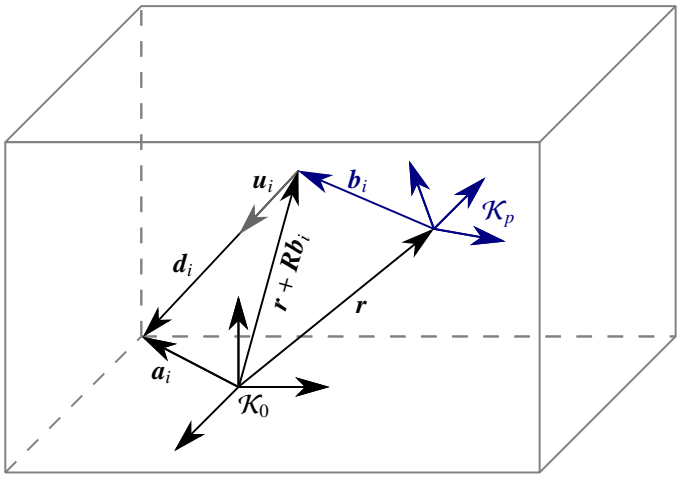

Figure 2: Illustration of the vectors associated with cable i

The cable directions $\boldsymbol{u}_i$ are used to assemble the structure matrix $\boldsymbol{A}^\mathsf{T} \in \mathbb{R}^{n \times m}$ of the CDPR. Each column $\boldsymbol{A}_i^\mathsf{T}$ of this matrix encapsulates the direction in which the i-th cable exerts a force and moment on the platform

$$\boldsymbol{A}_i^\mathsf{T} = \begin{bmatrix} \boldsymbol{u}_i \\ \boldsymbol{R}\boldsymbol{b}_i \times \boldsymbol{u}_i \end{bmatrix} \in \mathbb{R}^6. \tag{2}$$

The vector of cable forces $\boldsymbol{f} = \begin{bmatrix} f_1 & \cdots & f_m \end{bmatrix} \in \mathbb{R}^m$, which pull on the platform, is multiplied with $\boldsymbol{A}^\mathsf{T}$ to formulate the wrench equilibrium equation

$$\boldsymbol{A}^\mathsf{T}\boldsymbol{f} + \boldsymbol{g} = \boldsymbol{0}\,. \tag{3}$$

The platform's wrench due to gravity is denoted as $\boldsymbol{g} \in \mathbb{R}^6$.
Cable force distributions $\boldsymbol{f}$ are called feasible if they satisfy the wrench equilibrium in Equation (3) and the predefined limits

$$f_{\min} \le \boldsymbol{f}_i \le f_{\max} \qquad \text{for all } i \in \{1, ..., m\}\,. \tag{4}$$

The upper limit $f_{\max}$ is usually imposed by the capabilities of the CDPR's motors and winches. The lower limit $f_{\min} > 0$ is chosen sufficiently large to prevent cable sagging or coiling errors on the winches.
Redundantly-constrained CDPRs ($m > n$) are usually designed such that the structure matrix $\boldsymbol{A}^\mathsf{T}$ has full rank n within the desired workspace. As a result, the linear system in Equation (3) is underdetermined and has infinitely many solutions $\boldsymbol{f}^*$ which can be split into two components [2]

$$\boldsymbol{f}^* = -\boldsymbol{A}^{\mathsf{T}+}\boldsymbol{g} + \boldsymbol{N}\boldsymbol{\alpha}\,. \tag{5}$$

The first term $-\boldsymbol{A}^{\mathsf{T}+}\boldsymbol{g}$ is the least-squares solution, which is calculated using the pseudo-inverse $\boldsymbol{A}^{\mathsf{T}+}$ of the structure matrix. The second term $\boldsymbol{N}\boldsymbol{\alpha}$ represents the position $\boldsymbol{\alpha} \in \mathbb{R}^{(m-n)}$ of the solution $\boldsymbol{f}^*$ within an arbitrary basis $\boldsymbol{N} \in \mathbb{R}^{m \times (m-n)}$ for the nullspace of the structure matrix. By definition, any value of $\boldsymbol{\alpha}$ fulfills the wrench equilibrium in Equation (3), but only those $\boldsymbol{\alpha}$ that also satisfy Equation (4) are considered feasible. This property is exploited by the new force control method presented in Section 3.

2.1. Dynamic Model

To validate the proposed control approach in simulation, a dynamic CDPR model is constructed by augmenting the wrench equilibrium from Equation (3). The platform's Newton–Euler equation of motion is given by

$$\boldsymbol{M}\ddot{\boldsymbol{x}} + \boldsymbol{C}\dot{\boldsymbol{x}} = \boldsymbol{A}^\mathsf{T}\boldsymbol{f} + \boldsymbol{g}\,, \tag{6}$$

where $\boldsymbol{M} \in \mathbb{R}^{6\times6}$ is the inertia matrix of the platform, that is multiplied by its acceleration $\ddot{\boldsymbol{x}}$. The matrix $\boldsymbol{C} \in \mathbb{R}^{6\times6}$ represents the influence of Coriolis and centripetal forces.
The cables are modeled as a Kelvin–Voigt material. This dynamic model is often used for the cables of CDPRs, as it offers a good representation of their short-term dynamics [38, page 159]. The model consists of a linear spring and a damping element arranged in parallel. The force $\boldsymbol{f}_i$ in each cable $i \in \{1, ..., m\}$ is calculated as a function of the cable length $\boldsymbol{l}_i$ from Equation (1), the rotational positions of the motors $\boldsymbol{\theta} \in \mathbb{R}^m$, and their derivatives

$$\boldsymbol{f}_i = k_c\left(\frac{\boldsymbol{l}_i}{r_w\boldsymbol{\theta}_i} - 1\right) + \eta\frac{\dot{\boldsymbol{l}}_i}{r_w\dot{\boldsymbol{\theta}}_i}. \tag{7}$$

Hereby, k_c is the stiffness of the spring, η is the viscosity of the damping element, and r_w is the effective radius of the winch.
The torque $\boldsymbol{\tau} \in \mathbb{R}^m$ generated by the winches is calculated based on their rotational state $\boldsymbol{\theta}$ and the cable forces $\boldsymbol{f}$

$$\boldsymbol{\tau} = \boldsymbol{J}\ddot{\boldsymbol{\theta}} + \boldsymbol{\nu}\dot{\boldsymbol{\theta}} + r_w\boldsymbol{f}. \tag{8}$$

The dynamic properties of the winches are captured in the diagonal inertia and viscous friction matrices $\boldsymbol{J}, \boldsymbol{\nu} \in \mathbb{R}^{m\times m}$, respectively.

3. Force Control in the Nullspace

The presented force control in the nullspace (FCN) for redundantly-constrained CDPRs is designed as an add-on to a simple control scheme based on an inverse kinematic model (IK). The latter calculates desired cable lengths $\boldsymbol{l}$ corresponding to the desired platform pose $(\boldsymbol{r}, \boldsymbol{R})$. In the joint space, built-in controllers of the servomotors that drive the CDPR's winches are responsible for reaching these desired cable lengths.
When the FCN method is activated, it adds offsets $\Delta\boldsymbol{l}$ to the desired cable lengths $\boldsymbol{l}$ before they are passed to the servomotors in the winches. The goals of the FCN method, in order of increasing priority, are:

1. The cable forces $\boldsymbol{f}$ should be kept as close as possible to the force level f_{ref}, which can be freely chosen within the limits from Equation (4).
2. The cable forces $\boldsymbol{f}$ should be within the limits of Equation (4).
3. The platform pose $(\boldsymbol{r}, \boldsymbol{R})$ should not be altered.

Figure 3 shows the structure of the proposed method as a block diagram. All blocks are repeatedly executed by the control system of the CDPR.

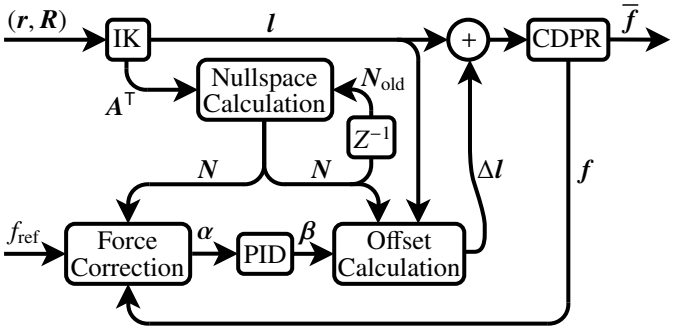

Figure 3: Structure of the Proposed Force Control Method

The FCN method first calculates a basis $\boldsymbol{N}$ for the nullspace of the structure matrix $\boldsymbol{A}^\mathsf{T}$. This basis is then used for the calculation of $\boldsymbol{\alpha}$ and the offsets $\Delta\boldsymbol{l}$ in order to satisfy the third goal of the FCN method. The desired force correction $\boldsymbol{\alpha}$ is calculated within the nullspace basis $\boldsymbol{N}$ in pursuit of the first two goals of the FCN method. The proportional-integral-derivative (PID) controller tries to move $\boldsymbol{\alpha}$ to zero by means of its output $\boldsymbol{\beta}$, which is also interpreted as a position in the nullspace. This output is translated to cable length offsets $\Delta\boldsymbol{l}$, which are added to the cable lengths $\boldsymbol{l}$ calculated by the inverse kinematic.
The following sections explain the function of the blocks in Figure 3 in detail.

3.1. Inverse Kinematics

The inverse kinematic block IK maps the desired platform pose $(\boldsymbol{r}, \boldsymbol{R})$ to corresponding cable lengths $\boldsymbol{l}$. It uses the pulley kinematic model developed in [39], which is applicable to the IPAnema Mini CDPR. The cables are considered to be straight lines originating from pulleys pivoting around proximal anchor points $\boldsymbol{a}_i$. Their elasticity and weight are neglected. The model also calculates the structure matrix $\boldsymbol{A}^\mathsf{T}$ at the current platform pose and passes it to the nullspace calculation block.

3.2. Nullspace Calculation

The nullspace calculation block computes a nullspace basis $\boldsymbol{N}$ for the structure matrix $\boldsymbol{A}^\mathsf{T}$, which is a continuous function of the pose $(\boldsymbol{r}, \boldsymbol{R})$. The essential property of continuity is not guaranteed when using standard nullspace calculation algorithms, as the calculated basis can be arbitrarily oriented within the nullspace. This free choice on behalf of the algorithm can introduce discontinuous jumps when the parameters of $\boldsymbol{A}^\mathsf{T}$ change. The necessary steps to ensure continuity are described as pseudocode in Algorithm 1.

Algorithm 1: Nullspace Calculation

Input: structure matrix $\boldsymbol{A}^\mathsf{T} \in \mathbb{R}^{n\times m}$,
previous nullspace basis $\boldsymbol{N}_{\text{old}} \in \mathbb{R}^{m\times(m-n)}$

1 $\tilde{\boldsymbol{N}} = \text{Nullspace}\left(\boldsymbol{A}^\mathsf{T}\right) \in \mathbb{R}^{m\times(m-n)}$

2 $\boldsymbol{U}, \boldsymbol{\Sigma}, \boldsymbol{V} = \text{SVD}\left(\tilde{\boldsymbol{N}}^\mathsf{T}\boldsymbol{N}_{\text{old}}\right)$

3 $\boldsymbol{N} = \tilde{\boldsymbol{N}}\boldsymbol{U}\boldsymbol{V}$

Output: continuous nullspace basis $\boldsymbol{N}$

The algorithm receives the nullspace basis from the previous cycle $\boldsymbol{N}_{\text{old}}$ as an input from the delay block which is labeled Z^{-1} in Figure 3. In Line 1, a nullspace basis of $\boldsymbol{A}^\mathsf{T}$ is calculated. To remove possible discontinuities in the basis' orientation, a coordinate transformation between the nullspace basis from the previous cycle $\boldsymbol{N}_{\text{old}}$ and the current one $\tilde{\boldsymbol{N}}$ is calculated. If the nullspace itself changes between two executions of Algorithm 1, the transformation $\tilde{\boldsymbol{N}}^\mathsf{T}\boldsymbol{N}_{\text{old}}$ is not an orthogonal matrix and has singular values smaller than 1. Applying $\boldsymbol{N} = \tilde{\boldsymbol{N}}\tilde{\boldsymbol{N}}^\mathsf{T}\boldsymbol{N}_{\text{old}}$ would avoid discontinuities in $\boldsymbol{N}$, but the resulting matrix is not an orthonormal basis of the nullspace as the norms of its column vectors would be smaller than 1. To correct this, Algorithm 1 instead uses the nearest orthogonal matrix of this transformation. This approximation is calculated using the singular value decomposition $\boldsymbol{U}\boldsymbol{\Sigma}\boldsymbol{V} = \tilde{\boldsymbol{N}}^\mathsf{T}\boldsymbol{N}_{\text{old}}$ in Line 2.
In practice, the nullspace changes only in small steps between two executions of Algorithm 1, even when the platform is moving at a high velocity. Therefore, all singular values of $\tilde{\boldsymbol{N}}^\mathsf{T}\boldsymbol{N}_{\text{old}}$ are always close to 1 and $\boldsymbol{U}\boldsymbol{V}$ is a sufficiently close orthogonal approximation of $\boldsymbol{U}\boldsymbol{V} \approx \tilde{\boldsymbol{N}}^\mathsf{T}\boldsymbol{N}_{\text{old}}$.
The matrix $\boldsymbol{N}$, as calculated in Line 3, is an orthonormal basis of the nullspace and a continuous function of the platform pose $(\boldsymbol{r}, \boldsymbol{R})$.

3.3. Force Correction

The force correction block in Figure 3 calculates the desired change in the cable forces in order to achieve the three goals of the FCN method. To address the first goal, the cable forces $\boldsymbol{f}$ are shifted

$$\widehat{\boldsymbol{f}} = \boldsymbol{f} - f_{\text{ref}}\mathbf{1}\,, \tag{9}$$

such that the objective can be stated as $\widehat{\boldsymbol{f}} = \mathbf{0}$. Hereby, $\mathbf{1} \in \mathbb{R}^m$ denotes the vector whose components are all 1. To move towards its first goal, the FCN method changes the cable force in the direction $\Delta \boldsymbol{f}$ with

$$\Delta \boldsymbol{f} = -\widehat{\boldsymbol{f}}. \tag{10}$$

If the forces are not within their limits from Equation (4), achieving this state becomes a higher priority than the force level f_{ref}. The direction of the force changes $\Delta \boldsymbol{f}$ is subsequently skewed towards the cable which violates its limits the most. This shift between the first two goals is implemented by raising the vector $\widehat{\boldsymbol{f}}$ to the power $p \geq 1$ while preserving its sign

$$\widehat{\boldsymbol{f}}^p = \begin{bmatrix} \operatorname{sign}\left(\widehat{f}_1\right) \left|\widehat{f}_1\right|^p & \cdots & \operatorname{sign}\left(\widehat{f}_m\right) \left|\widehat{f}_m\right|^p \end{bmatrix}^{\mathsf{T}}. \tag{11}$$

The power $p \in \mathbb{R}$ is a function of the largest cable force limit violation

$$p = 1 + p_{\text{scale}} \cdot \max \left\{ \begin{matrix} 0, \\ \max\limits_{i=1,\dots,m} \left(\boldsymbol{f}_i - f_{\max}\right), \\ \max\limits_{i=1,\dots,m} \left(f_{\min} - \boldsymbol{f}_i\right) \end{matrix} \right\}. \tag{12}$$

The slope parameter p_{scale} determines how quickly the controller changes its priority from the first to the second objective when cable forces start to violate their limits. While the vector from Equation (11) determines the direction in which the cable forces are changed, the magnitude of this change is scaled linearly with the distance $\|\widehat{\boldsymbol{f}}\|$ from f_{ref}. Finally, the desired change of the cable forces $\Delta \boldsymbol{f}$ can be calculated as

$$\Delta \boldsymbol{f} = -\frac{\left\|\widehat{\boldsymbol{f}}\right\|}{\left\|\widehat{\boldsymbol{f}}^p\right\|} \widehat{\boldsymbol{f}}^p. \tag{13}$$

Notice that if the second goal is satisfied, $p = 1$ according to Equation (12) and the force changes $\Delta \boldsymbol{f}$ from Equations (10) and (13) are the same. Therefore, an explicit distinction between the cases $p > 1$ and $p = 1$ is not necessary.

To gain a better understanding for the behavior of Equation (13), $\Delta \boldsymbol{f}$ is visualized in Figure 4 as a vector field for the two-dimensional case with $m = 2$. Hereby, f_{ref} is set to be the average of the force limits. This visualization shows how $\Delta \boldsymbol{f}$ is a continuous function of the cable forces $\boldsymbol{f}$.

To satisfy the third goal of not altering the platform pose $(\boldsymbol{r}, \boldsymbol{R})$, the desired force change $\Delta \boldsymbol{f}$ is projected onto the nullspace of the structure matrix $\boldsymbol{A}^{\mathsf{T}}$ at the current pose

$$\boldsymbol{\alpha} = \boldsymbol{N}^{\mathsf{T}} \Delta \boldsymbol{f}. \tag{14}$$

The resulting vector $\boldsymbol{\alpha} \in \mathbb{R}^{(m-n)}$ is the position of the desired force changes within the nullspace basis $\boldsymbol{N} \in \mathbb{R}^{m \times (m-n)}$.

The previously described steps of the force correction block are summarized in Algorithm 2 as pseudocode.

3.4. PID Controller

The PID block in Figure 3 contains a proportional-integral-derivative controller, whose goal is to drive $\boldsymbol{\alpha} \in \mathbb{R}^{(m-n)}$ to zero

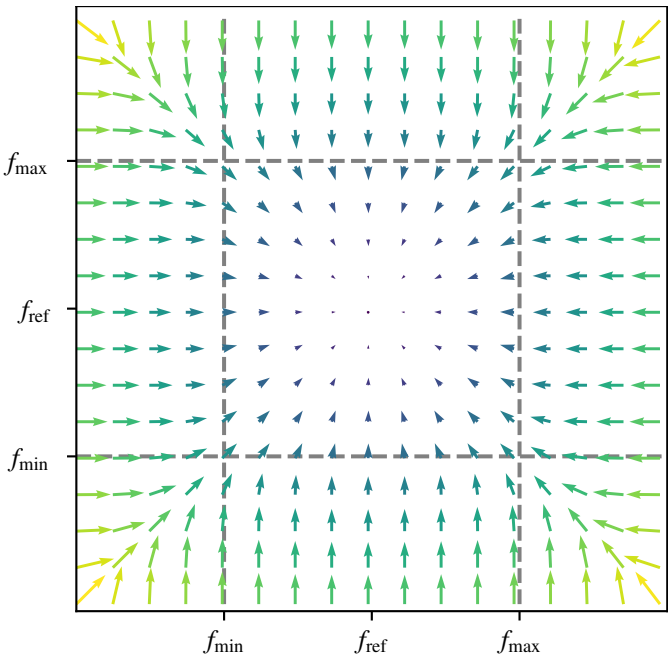

Figure 4: Two-Dimensional Visualization of $\Delta \boldsymbol{f} \in \mathbb{R}^2$ for All Cable Forces $\boldsymbol{f} \in \mathbb{R}^2$

Algorithm 2: Force Correction

Input: cable forces $\boldsymbol{f} \in \mathbb{R}^m$, force level f_{ref}, nullspace basis $\boldsymbol{N} \in \mathbb{R}^{m \times (m-n)}$

1 $\widehat{\boldsymbol{f}} = \boldsymbol{f} - f_{\text{ref}} \mathbf{1}$

2 $p = 1 + p_{\text{scale}} \cdot \max \left\{ \begin{matrix} 0, \\ \max\limits_{i=1,\dots,m} \left(\boldsymbol{f}_i - f_{\max}\right), \\ \max\limits_{i=1,\dots,m} \left(f_{\min} - \boldsymbol{f}_i\right) \end{matrix} \right\}$

3 $\Delta \boldsymbol{f} = -\frac{\left\|\widehat{\boldsymbol{f}}\right\|}{\left\|\widehat{\boldsymbol{f}}^p\right\|} \widehat{\boldsymbol{f}}^p$

4 $\boldsymbol{\alpha} = \boldsymbol{N}^{\mathsf{T}} \Delta \boldsymbol{f}$

Output: desired nullspace position $\boldsymbol{\alpha}$

by adjusting its output $\boldsymbol{\beta} \in \mathbb{R}^{(m-n)}$. The controller has a diagonal structure and takes the form $\boldsymbol{R}(s) = R(s)\,\boldsymbol{I}$ in the Laplace domain. Hereby, $\boldsymbol{I} \in \mathbb{R}^{(m-n)\times(m-n)}$ denotes an identity matrix and $R(s)$ is the transfer function

$$R(s) = K_p + \frac{K_i}{s} + K_d s\,, \tag{15}$$

where the proportional K_p, integral K_i, and derivative K_d gains are chosen using the following procedure.
The FCN method's first goal of bringing all cable forces as close to f_{ref} as possible also implies that their average $\overline{f}$ moves to this level. For a fixed platform pose $(\boldsymbol{r}, \boldsymbol{R})$, and only for controller tuning purposes, let us consider all blocks from Figure 3 as a single-input single-output time-invariant linear system $M(s)$ with the input f_{ref} and output $\overline{f}$. This is assumed to be equivalent to a simple unity-feedback system with f_{ref} being the set-point variable and $\overline{f}$ the controlled variable yielding

$$M(s) = \frac{R(s)G(s)}{1 + R(s)G(s)} \tag{16}$$

where $R(s)$ represents the PID controller and $G(s)$ is the collection of all other blocks in Figure 3. The first step in tuning the controller is to approximate the transfer function $M(s)$ based on its time response. To obtain this data, the controller is restricted to contain only a proportional term $R(s) = K_p$ with an appropriate value such that $\overline{f}$ exhibits several oscillations after a step increase of f_{ref}. Although the dynamics of CDPRs are known to be highly non-linear, modeling $M(s)$ as a linear system allows using a black box identification technique [40], which simplifies the tuning procedure. From the identified system $M(s)$, which includes the proportional controller, the transfer function $G(s)$ can be calculated using Equation (16). The well-known frequency response tuning technique is employed to obtain a PID controller $R(s)$, yielding an open loop transfer function $H(s) = R(s)G(s)$ with desired properties. Based on definitions from [41, page 464], the following relationships are established for the system's gain crossover frequency ω_{gc}, phase crossover frequency ω_{pc}, phase margin ϕ_m, and gain margin K_g

$$\Re\left\{R\left(j\omega_{gc}\right)\right\} = K_p\,, \tag{17}$$

$$\Im\left\{R\left(j\omega_{gc}\right)\right\} = K_d\omega_{gc} - \frac{K_i}{\omega_{gc}}\,. \tag{18}$$

Hereby, $R(j\omega_{gc}) = -e^{j\phi_m}/G(j\omega_{gc})$ is the value of the controller in the frequency domain. While the value of K_p is determined by Equation (17), one degree of freedom remains for K_d and K_i whose relationship is established in Equation (18). This can be resolved by setting a convenient value for the pair (K_g, ω_{pc}).

3.5. Offset Calculation

The offset calculation block in Figure 3 translates the nullspace position $\boldsymbol{\beta} \in \mathbb{R}^{(m-n)}$ into cable length offsets $\Delta\boldsymbol{l} \in \mathbb{R}^m$. It assumes that the cables behave similarly to linear springs when changes in the cable forces $\boldsymbol{N\beta}$ are converted to changes in the cable lengths. The stiffness of the cables is assumed to be proportional to their lengths $\boldsymbol{l}$ divided by a specific stiffness constant k_c that depends on the cables' material and diameter. The cable length offsets $\Delta\boldsymbol{l} \in \mathbb{R}^m$ are calculated as

$$\Delta\boldsymbol{l} = \frac{1}{k_c}\operatorname{diag}(\boldsymbol{l})\,\boldsymbol{N\beta}\,, \tag{19}$$

where $\operatorname{diag}(\boldsymbol{l})$ is the diagonal matrix whose entries are the components of $\boldsymbol{l}$. The assumptions underlying Equation (19) are simplifications and might not be true in practice. Nevertheless, this equation provides a sufficient approximation of the cables' behavior for the FCN method to work as shown in Section 4. Modeling errors concerning the cables' behavior and elasticity (e.g. a wrong value of k_c) can be compensated in practice by tuning the gains of the controller.

3.6. CDPR

The CDPR block in Figure 3 represents the robot's behavior which follows the commanded cable lengths $\boldsymbol{l} + \Delta\boldsymbol{l}$ using the servomotors in its winches. The resulting cable forces $\boldsymbol{f}$ are measured and passed to the force correction block. For the purpose of tuning the PID controller as described in Section 3.4, the average cable force $\overline{f} \in \mathbb{R}$ is calculated and provided as an output

$$\overline{f} = \frac{1}{m}\sum_{i=1}^{m} \boldsymbol{f}_i\,. \tag{20}$$

4. Evaluation in Simulations and Experiments

The simulations and experiments in this work are performed with the IPAnema Mini at Fraunhofer IPA [1, page 398]. It is a redundantly-constrained CDPR with $m = 8$ cables and $n = 6$ degrees-of-freedom, which is shown in Figure 1. Its geometry parameters $\boldsymbol{a}_i$ and $\boldsymbol{b}_i$ are listed in Table 1.

Table 1: IPAnema Mini Geometry

i	$\boldsymbol{a}_i$ [mm]			$\boldsymbol{b}_i$ [mm]		
1	[500.0	− 377.5	447]	[22	− 40	− 82.5]
2	[−500.0	− 378.0	447]	[−22	− 40	− 82.5]
3	[−500.0	378.0	447]	[−22	40	− 82.5]
4	[500.0	377.5	447]	[22	40	− 82.5]
5	[531.5	− 344.5	− 447]	[22	− 40	82.5]
6	[−531.5	− 344.5	− 447]	[−22	− 40	82.5]
7	[−531.5	344.5	− 447]	[−22	40	82.5]
8	[531.5	344.5	− 447]	[22	40	82.5]

The IPAnema Mini uses Dyneema cables with a diameter of 1.5 mm and a specific stiffness of $k_c = 28500\,\text{N}$ [1, page 398]. The viscosity of the cables in the dynamic simulation model Section 2.1 is set to $\eta = 200\,\text{N}$. The winches are dimensioned for cable forces of up to 40 N. For the purpose of this work, the cable force limits are set to $f_{\min} = 10\,\text{N}$ and $f_{\max} = 25\,\text{N}$.

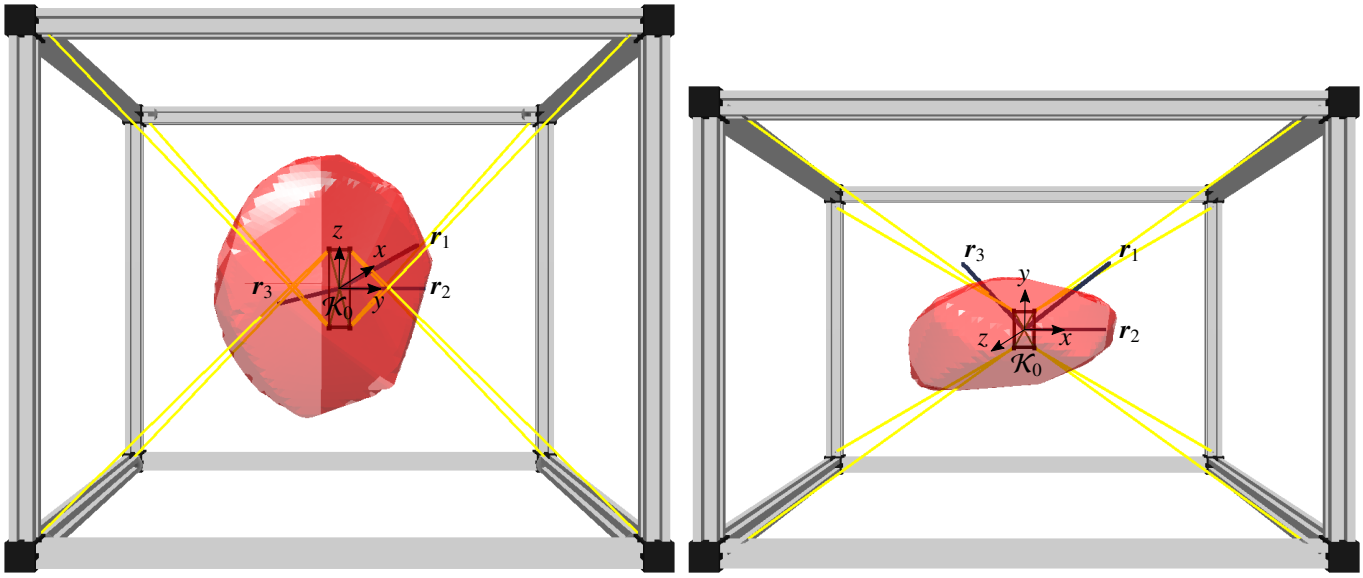

Figure 5: Visualization of the IPAnema Mini with its wrench-feasible workspace (red) and trajectory endpoints $\boldsymbol{r}_1, \boldsymbol{r}_2, \boldsymbol{r}_3$ from two perspectives.

These restrictive limits are purposefully chosen to investigate the behavior of the control methods when the platform leaves the wrench-feasible workspace defined by these limits. The IPAnema Mini's platform weighs 0.25 kg. Its control system is based on the TwinCAT 3.1 software by Beckhoff and runs on a programmable logic control (PLC) with a cycle time of 1 millisecond.

For the experiments in Section 4.3, the platform's position is measured with a Leica AT960 laser tracker and a target as shown in Figure 1. This laser tracker can measure the target's position with an absolute accuracy of $\pm\left(15\,\mu\text{m} + 6\,\frac{\mu\text{m}}{\text{m}}\right)$, which decreases by $6\,\mu$m per meter distance from the target. For the static experiments in this work, the laser tracker was placed three meters away from the center of the workspace of the IPAnema Mini, which implies an absolute measurement accuracy of $\pm 33\,\mu$m. The sampling rate of these measurements is 1000 Hz.

The experiments and simulations in this work are conducted at three different platform positions and on three linear trajectories dispersed throughout the IPAnema Mini's workspace.

The trajectories start at the origin $\boldsymbol{r}_0 = \boldsymbol{0}$ in the fixed coordinate system $\mathcal{K}_0$, in the center of the frame, and end at the points

$$\boldsymbol{r}_1 = \begin{bmatrix} 180\,\text{mm} \\ 140\,\text{mm} \\ 100\,\text{mm} \end{bmatrix}, \quad \boldsymbol{r}_2 = \begin{bmatrix} 180\,\text{mm} \\ 0\,\text{mm} \\ 0\,\text{mm} \end{bmatrix}, \quad \boldsymbol{r}_3 = \begin{bmatrix} -140\,\text{mm} \\ 150\,\text{mm} \\ -35\,\text{mm} \end{bmatrix}. \tag{21}$$

The platform orientation remains the same $\boldsymbol{R} = \boldsymbol{I} \in \text{SO}(3)$ for all simulations and experiments.

Figure 5 shows renderings of the IPAnema Mini and these trajectories from two perspectives created with the open-source CDPR simulation software WireX [42]. The volume of its static wrench-feasible workspace is depicted in red. It is calculated for the force limits from Equation (4), using the force distribution method from [43]. The platform wrench $\boldsymbol{g} = -\boldsymbol{A}^\mathsf{T}\boldsymbol{f}$, used for this computation, is calculated from the measured cable forces $\boldsymbol{f}$ at the position $\boldsymbol{r}_0$.

Figure 5 shows that the point $\boldsymbol{r}_2$ lies within this workspace, while $\boldsymbol{r}_1$ and $\boldsymbol{r}_3$ do not. On the straight lines from $\boldsymbol{r}_0$ through the points $\boldsymbol{r}_1, \boldsymbol{r}_2, \boldsymbol{r}_3$, the workspace ends after 155 mm, 182 mm, 127 mm, respectively.

The following sections discuss the tuning of the FCN controller for the IPAnema Mini and its comparison to state-of-the-art controllers in simulation and experiments.

4.1. Controller Tuning

The PID controller within the FCN method is tuned according to the procedure from Section 3.4. The parameter p_{scale}, which controls how quickly the FCN method shifts between its first two goals, is set to $p_{\text{scale}} = 2$. This choice is a compromise between how quickly the controller can shift its priorities and its robustness at the borders of the workspace.

The design values used for the tuning are $\omega_{gc} = 17.6\,\text{rad/s}$ and $\phi_m = 80°$. The value of ω_{gc} is selected such that the controlled system is 14 times faster than the open-loop system, based on the approximate formula $\omega_{gc} \approx \pi/t_s$, where t_s is the system's settling time. This is a compromise between the speed and robustness of the controller. Experiments show that larger values of ω_{gc} cause the system to be unstable at the borders of the workspace when $p > 1$.

A value of $K_i = 14.3$ is selected as a trade-off between speed and stability, yielding values of $K_g = 15.2\,\text{dB}$ and $\omega_{pc} = 194\,\text{rad/s}$. The resulting values for the remaining controller gains by means of Equations (17) and (18) are $K_p = 0.206$ and $K_d = 0.0063$.

4.2. Comparison to a MPC Method

The MPC method introduced by Santos et al. [20] is a state-of-the-art CDPR control method capable of pursuing multiple objectives at once. Following an optimal control approach, it

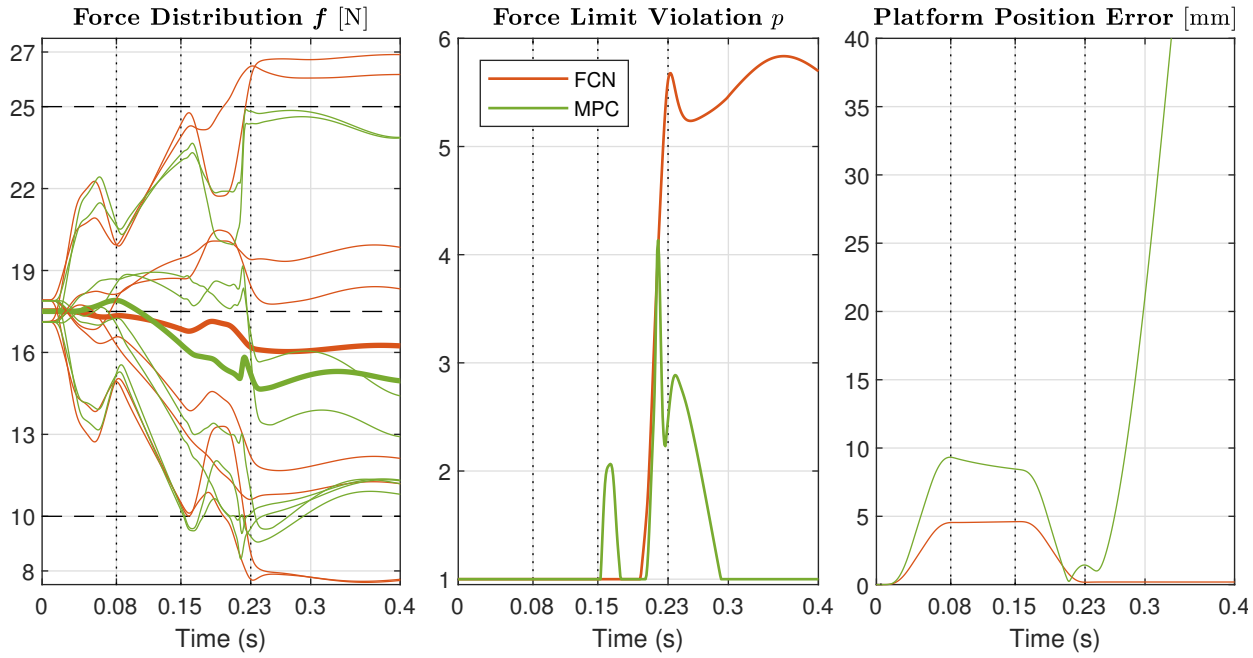

Figure 6: Simulation of the FCN and MPC Methods on the Third Trajectory with a Velocity of 1 m/s

specifies a quadratic program that minimizes a weighted sum of the CDPR's pose error, variation of its cable forces, and their norm $\|\boldsymbol{f}\|$. The feasibility of the cable forces from Equation (4) is mandated as an explicit constraint to the optimization problem. Therefore, the CDPR always remains within the wrench-feasible workspace, even when the commanded trajectory leaves it. This is a significant difference to the FCN method, which always follows the commanded trajectory even when the force limits are violated. To ensure a fair comparison between these methods within the wrench-feasible workspace of the CDPR, the third objective of the MPC method is altered to minimize $\|\widehat{\boldsymbol{f}}\|$ as defined in Equation (9) instead of $\|\boldsymbol{f}\|$.

This comparison is performed in simulation instead of experiments since implementing the MPC method on the IPAnema Mini CDPR would be very laborious, requiring the implementation of complex numerical solvers within its PLC. Furthermore, it is easier to ensure a fair comparison between the methods when using the dynamic model of the IPAnema Mini from Section 2.1 in MATLAB Simulink.

Simulations show that the methods behave similarly on all three trajectories from Figure 5. Therefore, only the third trajectory is analyzed in detail for a velocity of 1 m/s.

Figure 6 shows the evolution of the cable forces $\boldsymbol{f}$, force limit violations p, and deviations from the nominal trajectory of the FCN and MPC methods over time, during and after this trajectory. The dotted vertical lines indicate the acceleration and deceleration phases of the trajectory. Between the first two vertical lines, the CDPR moves with a constant platform velocity of 1 m/s. The first plots show that both controllers produce similar cable forces during the trajectory. The FCN method is slightly better at keeping them closer to their desired level f_{ref}, which can be observed from the cable force averages $\overline{\boldsymbol{f}}$, that are shown as thick lines. The second plot shows that the FCN method can also keep the cable forces feasible (i.e. $p = 1$) slightly longer than the MPC method. In terms of platform position error, the FCN is better than the MPC method due to the different priorities of the two methods and the fact that the FCN method only alters the cable forces within the nullspace. Once the trajectory has ended after 0.23 seconds, the MPC method moves the platform to a position where it can find feasible cable forces again. The computation times of the FCN and MPC methods during these simulations, performed in MATLAB Simulink, are measured and averaged over 50 executions. The FCN method is 79% faster than the MPC method. This significant difference in computational costs could be exploited to run the FCN controller at faster cycle times than MPC, enabling it to react more quickly to changes in the cable forces.

4.3. Disturbance Rejection

The ability of the FCN method to reject disturbances in the cable forces is evaluated in experiments at the center $\boldsymbol{r}_0$, near the border $\boldsymbol{r}_2$, and outside $\boldsymbol{r}_1$ of the wrench-feasible workspace shown in Figure 5.

For each pose, the same experiment is conducted with the IK and the FCN method. The platform is moved to one of the poses, and the cable forces settle into a stationary state. A mass of $w = 2.916\,\text{kg}$ is manually placed on the platform. After the system reaches a new disturbed stationary state, the additional weight is removed again. In these experiments, the robot shows qualitatively the same behavior at all three positions. Therefore, it is only analyzed in detail for $\boldsymbol{r}_0$ in Figure 7.

The force distribution plot shows the cable forces and their averages (thick lines) for the FCN and IK methods. The average of the FCN method shows its reaction to the disturbance. For the first 200 ms, it decreases similar to the IK method, but then it increases and stabilizes slightly above the desired level

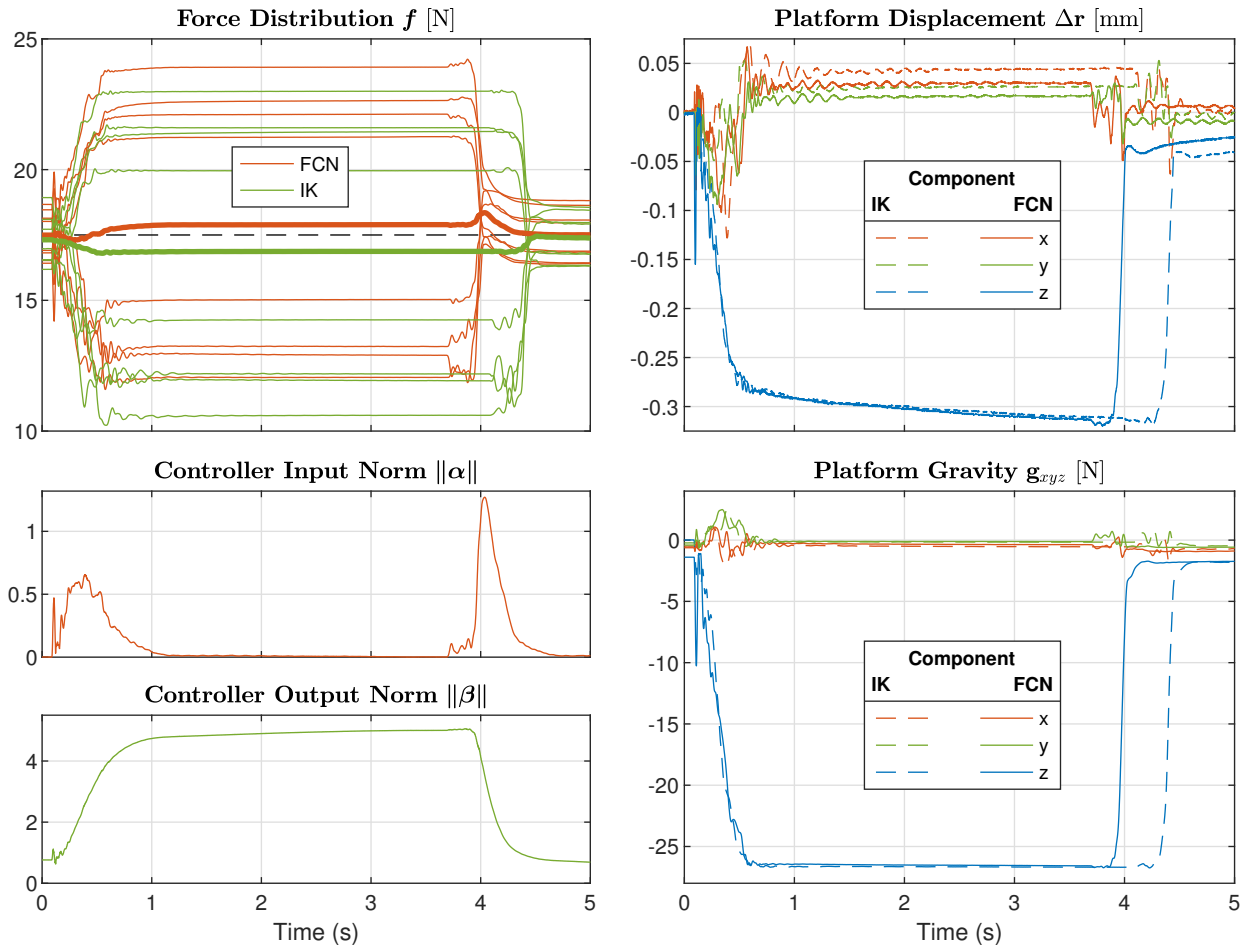

Figure 7: Measurements of the Disturbance Rejection Experiment in the Workspace Center $\boldsymbol{r}_0$

$f_{\text{ref}} = 17.5\,\text{N}$. After around four seconds, the weight is removed from the platform and the cable forces return to their previous levels.

The plots of the controller's input and output magnitudes show how quickly the FCN method reacts to the disturbance of the weight being placed on the platform. It takes around one second before the controller regains its desired state of $\|\boldsymbol{\alpha}\| = 0$ after the weight is placed on the platform. When it is removed again, this only takes half a second. This difference might be caused by the fact that the weight is manually placed and removed from the platform. Thus, the resulting wrench acting on the platform does not change instantaneously as the weight transitions between the hands of the experimenter and the platform. While the weight is resting on the platform, the magnitude of the controller output $\|\boldsymbol{\beta}\|$ slowly increases to counteract creep effects in the cables.

The platform displacement plot shows the relative change in the platform position $\Delta\boldsymbol{r}$ as measured by the laser tracker. We observe an identical behavior in $\Delta\boldsymbol{r}$ for both methods. This shows that the FCN method does not influence the stiffness of the platform at $\boldsymbol{r}_0$, as it does not significantly change the cable forces.

The fourth plot shows the relative changes in the first three components of the platform's gravity $\boldsymbol{g}_{xyz} \in \mathbb{R}^3$ due to the weight. This force is calculated based on the cables' measured forces $\boldsymbol{f}$ and directions $\boldsymbol{u}_i$ from Equation (1)

$$\boldsymbol{g}_{xyz} = -\sum_{i=1}^{m} \boldsymbol{u}_i \boldsymbol{f}_i \,. \tag{22}$$

Its plot shows an identical behavior for both methods. This is expected, as the force corrections of the FCN method are designed to be inside the nullspace of the structure matrix $\boldsymbol{A}^\mathsf{T}$.

The experimental results at all three platform positions from Equation (21) are summarized in Table 2. For each position and control method, the columns $\overline{\boldsymbol{f}}$ and $\overline{\boldsymbol{f}}_w$ contain the average cable force in the stationary state before and after the weight is placed on the platform, respectively. In all cases, the FCN method brings the average force closer to the desired level f_{ref} when compared to the IK method. This effect is stronger at the positions near the border $\boldsymbol{r}_2$ or outside $\boldsymbol{r}_1$ of the workspace. The columns p and p_w show the force limit violation defined in Equation (12) for the stationary states before and after the weight is placed on the platform. For $\boldsymbol{r}_1$ and $\boldsymbol{r}_2$, the FCN method significantly reduces the value of p relative to the IK method. The column $\|\Delta\boldsymbol{r}\|$ contains the total deviation of the platform's position due to the weight. This deviation depends on the stiffness of the platform, which in turn depends on the cable forces and their average level $\overline{\boldsymbol{f}}$. A high cable force average implies a high stiffness of the platform and therefore reduces the deviation $\|\Delta\boldsymbol{r}\|$ induced by the weight.

The experiments in this section show that the FCN method can quickly reject disturbances and keeps the cable forces close to their desired level f_{ref}. By adjusting this level, the FCN method could be used to indirectly modify the stiffness of the platform.

4.4. Workspace Investigation

The behavior of the IK and FCN methods is evaluated on the three trajectories presented in Figure 5 for the platform velocities $1/3\,\text{m/s}$, $2/3\,\text{m/s}$, and $1\,\text{m/s}$. The behavior is also investigated in the static workspace, i.e. at velocity $0\,\text{m/s}$. To measure this, the three trajectories are discretized into 50 poses, where measurements are taken after the CDPR has reached a stationary state. On each dynamic trajectory, the platform quickly accelerates from its resting position at $\boldsymbol{r}_0$ to reach one of the three previously mentioned velocities. It travels with this constant velocity for the majority of the trajectory until it decelerates to stop at $\boldsymbol{r}_1$, $\boldsymbol{r}_2$, or $\boldsymbol{r}_3$. The length of the acceleration and deceleration phases of the trajectories increases for higher velocities, with a maximum of 13.55 mm necessary for reaching $1\,\text{m/s}$. Hereby, the platform experiences a maximal acceleration of $27\,\text{m/s}^2$, reaching the limits of the IPAnema Mini's capabilities.

Figure 8 shows the influence of the platform's velocities on the average cable force $\overline{\boldsymbol{f}}$, force limit violation measure p, and the magnitudes of the controller's input $\|\boldsymbol{\alpha}\|$ and output $\|\boldsymbol{\beta}\|$. These values are plotted as a function of the distance along the three trajectories. After the platform stops at the endpoint of each trajectory, the values are recorded for an additional second to show how they reach a stationary state.

Comparing the two methods for the same velocity shows that the FCN method can keep $\overline{\boldsymbol{f}}$ closer to the desired level f_{ref} and p closer to 1 than the IK method. For the velocities $1/3\,\text{m/s}$, $2/3\,\text{m/s}$, and $1\,\text{m/s}$, the behavior of the IK method is almost identical, and only differs in the static experiments. The behavior of the FCN method changes with increasing velocities as its objectives become more challenging and its distance to them increases. After the platform stops at the end of the trajectories, the FCN method brings $\overline{\boldsymbol{f}}$ and p to a stationary state which is independent of the platform's previous velocity.

The plots of p in Figure 8 show how much of the IPAnema Mini's workspace is accessible to the controllers in practice. Similar to the observations in the prior work [29] on the IPAnema 3 CDPR, the static experiments show a good correspondence between the extent of the wrench-feasible workspace shown in Figure 5 and the portion of the trajectories in Figure 8 where $p = 1$ for the FCN method. On the first and third trajectories, the accessible workspace of the FCN method in the static case ends 26 mm before and 5 mm after the wrench-feasible workspace, respectively. The second trajectory is contained within the wrench-feasible workspace and the accessible one of the FCN method in the static experiments.

With increasing velocities, only smaller portions of the trajectories are within the accessible workspace of the controllers. Nevertheless, the FCN significantly decreases the force limit violation p compared to the IK method.

The plots of the magnitudes of the FCN method's controller input $\|\boldsymbol{\alpha}\|$ look similar for the velocities $1/3\,\text{m/s}$, $2/3\,\text{m/s}$ and $1\,\text{m/s}$. Once the platform stops at the end of each trajectory, it takes around half a second until the FCN method brings the controller input to its desired state $\|\boldsymbol{\alpha}\| = 0$. In the static experiments, $\|\boldsymbol{\alpha}\| = 0$ at every point of the trajectories because the measurements are recorded once the CDPR reaches a stationary state.

The plots of the magnitude of the controller output $\|\boldsymbol{\beta}\|$ show that it steadily increases along the trajectories. This increase is

Table 2: Static Experiments Results

Position	Method	$\overline{f}$ [N]	$\overline{f}_w$ [N]	p	p_w	$\|\|\Delta \boldsymbol{r}\|\|$ [mm]
$\boldsymbol{r}_0$	IK	17.32	16.87	1.0	1.0	0.312
	FCN	17.49	17.89	1.0	1.0	0.313
$\boldsymbol{r}_1$	IK	12.66	13.14	15.37	19.57	0.954
	FCN	14.76	15.47	6.1	15.87	0.427
$\boldsymbol{r}_2$	IK	28.68	27.84	27.48	33.96	0.316
	FCN	16.83	17.1	1.0	5.36	0.355

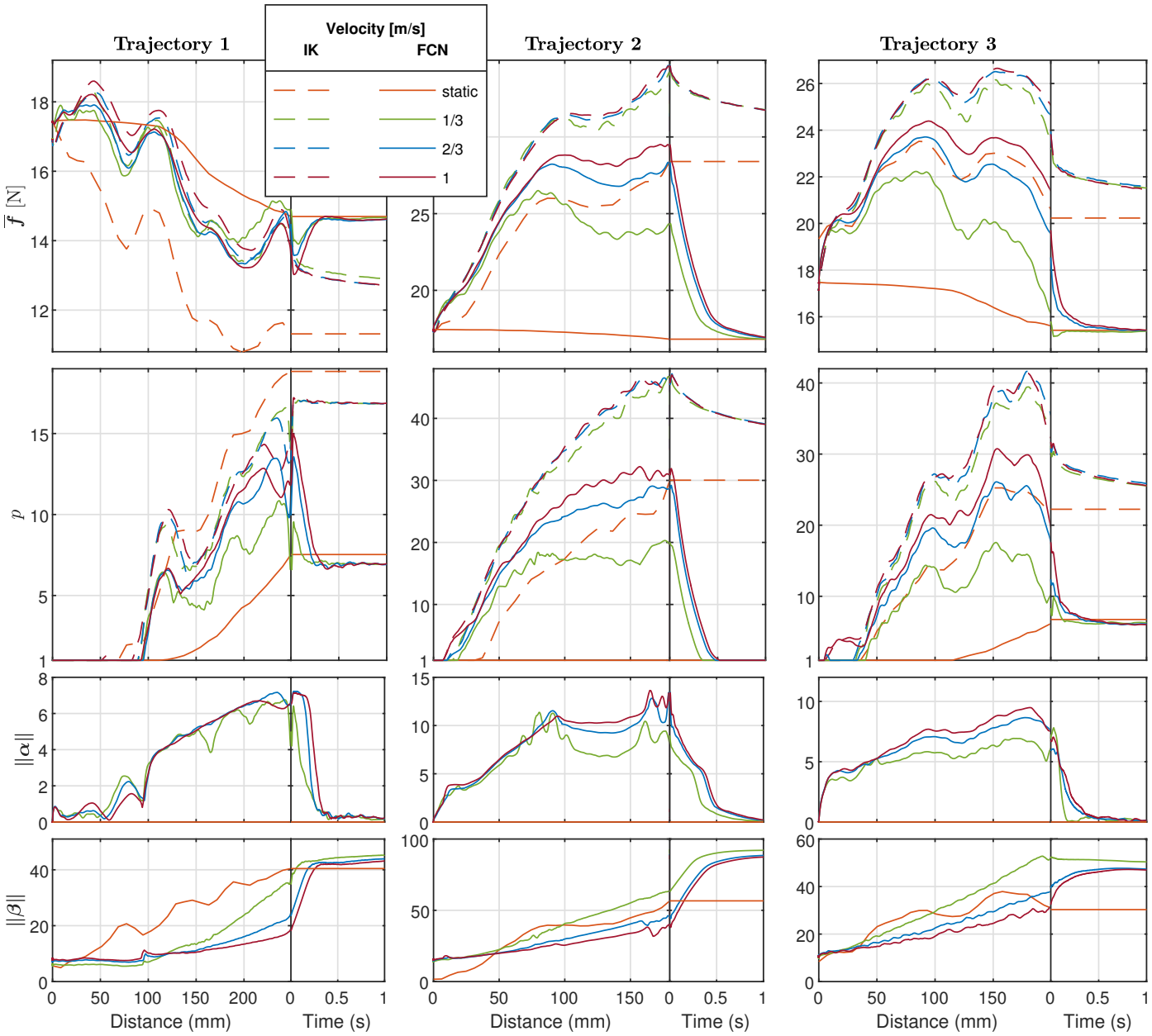

Figure 8: Behavior of the IPAnema Mini for Various Velocities During and After the Three Trajectories

quicker for slower velocities as the controller has more time to work towards its objectives.

5. Conclusion and Outlook

This work presents a force control method for redundantly-constrained CDPRs that can keep the cable forces within their limits and close to a specified force level. It does not require knowledge of model parameters that are difficult to measure or might change during the operation of a CDPR. The performance of the new method is evaluated when disturbances are applied to the cable forces and on different trajectories with platform velocities of up to 1 m/s on the IPAnema Mini CDPR. In simulations, the method shows similar behavior in the cable forces as a state-of-the-art MPC method while being simpler and requiring 79% less computational effort.

The experiments in this work show that the new method can quickly react to disturbances and can significantly improve the feasibility of the cable forces, especially for high platform velocities, compared to a purely kinematic control method.

Future research could investigate the behavior of this method on CDPRs with different geometric properties or sagging cables to analyze its performance and applicability for redundantly-constrained CDPRs in general. The implications of modifying the desired force level f_{ref} during the operation of the new control method could also be analyzed with regard to the CDPR's stiffness.

Acknowledgment

The authors wish to thank the University of Castilla-La Mancha and the European Social Fund for their financial support through the pre-doctoral funding [2019/451] and mobility grant for doctoral students 2020.

References

[1] A. Pott, Cable-Driven Parallel Robots: Theory and Application, Springer, 2018.

[2] R. Verhoeven, Analysis of the Workspace of Tendon-based Stewart Platforms, Ph.D. thesis, Universität Duisburg-Essen, 2006.

[3] A. Ming, T. Higuchi, Study on multiple degree-of-freedom positioning mechanism using wires. I: Concept, design and control, International Journal of The Japan Society for Precision Engineering 28 (1994) 131–138.

[4] M. A. Khosravi, H. D. Taghirad, Robust PID control of fully-constrained cable driven parallel robots, Mechatronics 24 (2014) 87–97.

[5] J. Lamaury, M. Gouttefarde, A. Chemori, P.-E. Hervé, Dual-space adaptive control of redundantly actuated cable-driven parallel robots, in: 2013 IEEE/RSJ International Conference on Intelligent Robots and Systems, IEEE, 2013, pp. 4879–4886.

[6] R. Chellal, L. Cuvillon, E. Laroche, Model identification and vision-based H_∞ position control of 6-dof cable-driven parallel robots, International Journal of Control 90 (2017) 684–701.

[7] X. Aguas, M. Herrera, O. Camacho, P. Leica, A sliding mode control for a planar 4-cable direct driven robot, in: 2018 International Conference on Information Systems and Computer Science (INCISCOS), IEEE, 2018, pp. 23–28.

[8] P. Ren, Y. Sun, Sliding mode set point control of a six-dof cable-suspended parallel robot with tension constraints and uncertain disturbances, in: ASME 2018 International Design Engineering Technical Conferences and Computers and Information in Engineering Conference, American Society of Mechanical Engineers, 2018.

[9] Y. Wang, K. Zhu, F. Yan, B. Chen, Adaptive super-twisting nonsingular fast terminal sliding mode control for cable-driven manipulators using time-delay estimation, Advances in Engineering Software 128 (2019) 113–124.

[10] M. Hamann, C. Ament, Model-based control of a planar 3-dof cable robot using exact linearization, in: International Conference on Cable-Driven Parallel Robots, Springer, 2021, pp. 260–270.

[11] T. Dallej, M. Gouttefarde, N. Andreff, R. Dahmouche, P. Martinet, Vision-based modeling and control of large-dimension cable-driven parallel robots, in: 2012 IEEE/RSJ International Conference on Intelligent Robots and Systems, IEEE, 2012, pp. 1581–1586.

[12] Z. Zake, F. Chaumette, N. Pedemonte, S. Caro, Control stability workspace for a cable-driven parallel robot controlled by visual servoing, in: International Conference on Cable-Driven Parallel Robots, Springer, 2021, pp. 284–296.

[13] S. Khalilpour, R. Khorrambakht, H. Taghirad, P. Cardou, Robust cascade control of a deployable cable-driven robot, Mechanical Systems and Signal Processing 127 (2019) 513–530.

[14] B. Zi, B. Duan, J. Du, H. Bao, Dynamic modeling and active control of a cable-suspended parallel robot, Mechatronics 18 (2008) 1–12.

[15] W. Kraus, Force control of cable-driven parallel robots, Ph.D. thesis, University of Stuttgart, 2016.

[16] J. Lamaury, M. Gouttefarde, Control of a large redundantly actuated cable-suspended parallel robot, in: 2013 IEEE International Conference on Robotics and Automation, IEEE, 2013, pp. 4659–4664.

[17] S. Abdelaziz, L. Barbé, P. Renaud, M. de Mathelin, B. Bayle, Control of cable-driven manipulators in the presence of friction, Mechanism and Machine Theory 107 (2017) 139–147.

[18] J. Bieber, D. Bernstein, M. Schuster, K. Wauer, M. Beitelschmidt, Motor current based force control of simple cable-driven parallel robots, in: International Conference on Cable-Driven Parallel Robots, Springer, 2021, pp. 271–283.

[19] J. C. Santos, M. Gouttefarde, A. Chemori, A nonlinear model predictive control for the position tracking of cable-driven parallel robots, IEEE Transactions on Robotics (2022).

[20] J. C. Santos, A. Chemori, M. Gouttefarde, Redundancy resolution integrated model predictive control of cdprs: concept, implementation and experiments, in: 2020 IEEE International Conference on Robotics and Automation (ICRA), IEEE, 2020, pp. 3889–3895.

[21] T. Reichenbach, K. Rausch, F. Trautwein, A. Pott, A. Verl, Velocity based hybrid position-force control of cable robots and experimental workspace analysis, in: International Conference on Cable-Driven Parallel Robots, Springer, 2021, pp. 230–242.

[22] S. Khalilpour, R. Khorrambakht, M. Harandi, H. Taghirad, P. Cardou, Robust dynamic sliding mode control of a deployable cable driven robot, in: Iranian Conference on Electrical Engineering (ICEE), IEEE, 2018, pp. 863–868.

[23] C. Reichert, K. Müller, T. Bruckmann, Robust internal force-based impedance control for cable-driven parallel robots, in: Cable-Driven Parallel Robots, Springer, 2015, pp. 131–143.

[24] W. Shang, B. Zhang, B. Zhang, F. Zhang, S. Cong, Synchronization control in the cable space for cable-driven parallel robots, IEEE Transactions on Industrial Electronics 66 (2018) 4544–4554.

[25] S. Fang, D. Franitza, M. Torlo, F. Bekes, M. Hiller, Motion control of a tendon-based parallel manipulator using optimal tension distribution, IEEE/ASME Transactions On Mechatronics 9 (2004) 561–568.

[26] S.-R. Oh, S. K. Agrawal, Cable suspended planar robots with redundant cables: Controllers with positive tensions, IEEE Transactions on Robotics 21 (2005) 457–465.

[27] Y.-Q. Zheng, Feedback linearization control of a wire-driven parallel support system in wind tunnels, in: Sixth International Conference on Intelligent Systems Design and Applications, 2006.

[28] Y. Wang, L. Liu, J. Chen, F. Ju, B. Chen, H. Wu, Practical robust control of cable-driven robots with feedforward compensation, Advances in Engineering Software 145 (2020) 102801.

[29] M. Fabritius, C. Martin, G. R. Gomez, W. Kraus, A. Pott, A practical

force correction method for over-constrained cable-driven parallel robots, in: International Conference on Cable-Driven Parallel Robots, Springer, 2021, pp. 117–128.
[30] S.-R. Oh, S. K. Agrawal, Generation of feasible set points and control of a cable robot, IEEE Transactions on Robotics 22 (2006) 551–558.
[31] R. Qi, M. Rushton, A. Khajepour, W. W. Melek, Decoupled modeling and model predictive control of a hybrid cable-driven robot (hcdr), Robotics and Autonomous Systems 118 (2019) 1–12.
[32] H. D. Taghirad, Y. B. Bedoustani, An analytic-iterative redundancy resolution scheme for cable-driven redundant parallel manipulators, IEEE Transactions on Robotics 27 (2011) 1137–1143.
[33] M. Hassan, A. Khajepour, Optimization of actuator forces in cable-based parallel manipulators using convex analysis, IEEE Transactions on Robotics 24 (2008) 736–740.
[34] M. Agahi, L. Notash, Redundancy resolution of wire-actuated parallel manipulators, Transactions of the Canadian Society for Mechanical Engineering 33 (2009) 561–573.
[35] M. Gouttefarde, J. Lamaury, C. Reichert, T. Bruckmann, A versatile tension distribution algorithm for n-dof parallel robots driven by $n+2$ cables, IEEE Transactions on Robotics 31 (2015) 1444–1457.
[36] M. Gouttefarde, J.-F. Collard, N. Riehl, C. Baradat, Geometry selection of a redundantly actuated cable-suspended parallel robot, IEEE Transactions on Robotics 31 (2015) 501–510.
[37] V. Mattioni, E. Idà, M. Carricato, Force-distribution sensitivity to cable-tension errors in overconstrained cable-driven parallel robots, Mechanism and Machine Theory 175 (2022) 104940.
[38] P. Tempel, Dynamics of cable-driven parallel robots with elastic and flexible, time-varying length cables, Stuttgart: Fraunhofer Verlag, 2019.
[39] A. Pott, Influence of pulley kinematics on cable-driven parallel robots, in: Latest Advances in Robot Kinematics, Springer, 2012, pp. 197–204.
[40] L. Ljung, Black-box models from input-output measurements, in: Imtc 2001. proceedings of the 18th ieee instrumentation and measurement technology conference. rediscovering measurement in the age of informatics (cat. no. 01ch 37188), volume 1, IEEE, 2001, pp. 138–146.
[41] K. Ogata, Modern control engineering, Prentice hall, 2010.
[42] A. Pott, Wirex – an open source initiative scientific software for analysis and design of cable-driven parallel robots (2019). doi:10.13140/RG.2.2.25754.70088.
[43] L. Mikelsons, T. Bruckmann, M. Hiller, D. Schramm, A real-time capable force calculation algorithm for redundant tendon-based parallel manipulators, in: 2008 IEEE International Conference on Robotics and Automation, IEEE, 2008, pp. 3869–3874.